Title: Climatology of Ionospheric Amplitude Scintillation on GNSS Signals at South American Sector During Solar Cycle 24

Author #1: Eduardo Perez Macho, Centro de Rádio Astronomia e Astrofísica at Universidade Mackenzie, Rua da Consolação 930, 01302-907, São Paulo, Brazil, eduardopmacho@gmail.com

Author #2: Emília Correia, Centro de Rádio Astronomia e Astrofísica at Universidade Mackenzie, Rua da Consolação 930, 01302-907, São Paulo, Brazil; and Instituto Nacional de Pesquisas Espaciais (INPE), Av dos Astronautas 1758, 12227-010, São José dos Campos, Brazil, ecorreia@craam.mackenzie.br

Author #3: Luca Spogli, Istituto Nazionale di Geofisica e Vulcanologia, Via di Vigna Murata 605, 00143, Rome, Italy; and SpacEarth Technology, Via di Vigna Murata 605, 00143, Rome, Italy, luca.spogli@ingv.it

Author #4: Marcio Tadeu de Assis Honorato Muella, Instituto de Pesquisa e Desenvolvimento (IP&D), Lab. de Física e Astronomia at Universidade do Vale do Paraíba (UNIVAP), Av Shishima Hifumi 2911, 12244-390, São José dos Campos, Brazil, mmuella@univap.br

Corresponding author: Eduardo Perez Macho

Abstract:

Scintillations are caused by ionospheric irregularities and can affect the propagation of trans-ionospheric radio signals. One way to understand and predict the impact of such irregularities on Global Navigation Satellite System (GNSS) signals is through the climatological behavior of the ionospheric scintillation indexes during the different phases of a solar cycle. In this work, we investigate the amplitude scintillation index S4 during the full solar cycle 24 at South American (SA) sector, that is featured by the Ionospheric Anomaly (EIA) and by the South Atlantic Magnetic Anomaly (SAMA). We also investigate the daily variation of S4 and two case studies during geomagnetic storms. The results show a significant intensification of amplitude scintillations at northern and southern crest of EIA, especially during the southern hemisphere's spring/summer seasons, with a higher increase during solar maximum, and after sunset. And particularly at the SAMA region, where the intensity of magnetic field lines is lower, the S_4 fluctuations are much higher.

Keywords:

scintillation, irregularities, ionosphere, GNSS, EIA, SAMA

Introduction

Radio signals that propagate through the ionosphere are subject to scintillations, which are rapid changes in their amplitude and/or phase, caused by ionospheric electron density irregularities. The ionospheric scintillations can affect the Global Navigation Satellite Systems (GNSS) signals, the High Frequency (HF) communication, and the satellites control systems (Yeh and Liu, 1982; Kintner et al., 2009). In the case of amplitude scintillations, the already low intensity of the fluctuating GNSS signals can drop to a level in which the receiver is unable to track it, causing navigation unavailability or reducing its accuracy (Conker et al, 2003; Spogli et al., 2013a). Amplitude scintillation is triggered by diffraction effects and it is ruled out by the Fresnel's filtering mechanism (e.g., Ghobadi et al., 2020 and references therein). According to this, irregularity having scale size below the Fresnel's scale for L-band signals (order of few hundreds of meters for L-band signals) when crossed by the plane-wave, act as new wave sources, resulting in an interference at receiver level (Wernik et al. 2003). Among the phenomena that can trigger the formation of such small-scale ionospheric irregularities are those embedded in the growth and decay process of equatorial plasma bubbles (EPBs) and those induced by particles' precipitation. The EPBs are large-scale ionospheric structures featured by depleted electron density with respect to the ambient ionosphere, which are usually developed after the local sunset at the magnetic equator. The EPBs also tend to propagate along the magnetic field lines towards the attained position of the daytime Equatorial Ionospheric Anomaly (EIA) crests, located at around 15-20° north and south of magnetic equator under solar maximum conditions, where they present larger amplitudes (De Rezende et al., 2007; Muella et al., 2017; Li et al., 2020). Conversely, the particle's precipitation can enhance the conductivity in the ionosphere, also generating GNSS scintillation-effective irregularities (e. g., Spogli et al., 2013b). At the South American (SA) sector, the region of main interest is the South Atlantic Magnetic Anomaly (SAMA), where the weakest geomagnetic field on Earth allows precipitations of energetic particles from the inner radiation belt down to the atmosphere (Abdu et al., 2005, Moro et al., 2012).

Several works have investigated the ionospheric scintillation at the SA sector at some periods of solar cycle 24, which has just ended (e.g., De Rezende et al., 2010; Sreeja et al., 2011; Bougard et al., 2013; Alfonsi et al., 2013; Spogli et al., 2013a, 2013b; Cesaroni et al., 2015, Khadka et al., 2016; Muella et al., 2017; Correia et al., 2018; Guo et al., 2019; De Paula et al., 2019; Oliveira et al., 2020). Some of these works are worthwhile to highlight. Alfonsi at el. (2013) provided a climatological picture of the scintillation occurrence from October 2010 to September 2011, during the ascending phase of solar cycle 24, at a station located at the southern crest of EIA in the Argentina sector, showing scintillation peaks during equinoxes in the post-sunset, and a minimum in the winter. Spogli et al. (2013b) investigated the amplitude and phase scintillation occurrence over Brazil in the period August–November 2011, by means of the Ground-Based Scintillation Climatology (GBSC) technique. They studied the scintillation recurrent features during the rising phase of the solar maximum, providing also evidence of the joint effect of the post-sunset EPB and SAMA in generating irregularities being scintillation-effective. A better focus of the scintillation climatology on the post-sunset hours (22:00-04:00 LT), by using a longer dataset and by also depicting the effect of the northern crest of the EIA is provided in Bougard et al. (2013). Cesaroni et al. (2015) investigated through GBSC the scintillation and Total Electron Content (TEC) data acquired in 2012 over Brazil and highlighted the relationship between intensity and variability of the TEC gradients and the occurrence of ionospheric amplitude scintillation under the southern crest of the EIA and the larger occurrence during equinoctial and summer months. Muella et al. (2017) investigated the climatology of ionospheric amplitude scintillation from 1997 to 2014 in Brazil over a station located at a latitude of the southern crest of the EIA, revealing that irregularities increase during solar maximum and are more frequent from September to March, with a peak in December, mainly during pre-midnight hours. The results also revealed that in addition to the solar cycle dependence, the occurrence climatology of scintillations is also modulated by the secular variation drifts in the magnetic dip equator. Ionospheric scintillation, in the worst cases, can lead to a complete Loss of signal Lock (LoL) in GNSS receivers. Over Brazil, Damaceno et al. (2020) investigated the climatology of

LoL events throughout the solar cycle 24, reporting a strong overlap with the scintillation climatology (LoL maxima at post-sunset, in correspondence with the expected position of the EIA southern crest, and during summer/equinox).

There are works that have investigated how the ionospheric scintillation behaves globally. Brahmanandam et al. (2012) used FORMOSAT-3/COSMIC (F3C) satellites for the solar minimum year of 2008 and verified the appearance of scintillations at low latitudes after the sunset hours until post-midnight during equinox and northern winter seasons, while no activity was found in the southern winter seasons. They also verified the absence of scintillations at high latitudes. Juan et al. (2018) used ground-based receivers during some selected days of the solar maximum years of 2014 and 2015 and found that the amplitude scintillation is not important at high latitudes for the accuracy of GNSS navigation, but at low latitude regions it produces a worsening in the navigation. Spogli et al. (2013a) illustrates a climatological picture through GBSC technique from high to low latitudes (including SA sector) during 2011, i.e., under raising solar activity. In that work, the relative importance of the amplitude and phase scintillation in the different magnetic latitudinal sectors and magnetic local times is evidenced and the sectors in which the scintillation due to SAMA and post-sunset EPB are highlighted as “ionospheric hot spots” (as per their Figure 7).

Investigations were also performed in other low latitude sectors of different continents. In Africa, Olwendo and Cilliers (2018) suggested that scintillation occurrences due to ionospheric irregularities are enhanced 1 to 2 hours after Local Time (LT) sunset and Tilahun (2020) showed that extreme scintillation starts around 19:00 LT and continued until midnight. Akala et al. (2015) reported the climatology of amplitude scintillations on Global Positioning System (GPS) signals during the minimum and ascending phases of solar cycle 24 (2009–2011) and illustrates how the highest scintillation occurrences is recorded during equinoxes and June solstice.

Over the Indian sub-continent, Goswami et al. (2017) found intense scintillations at the northern anomaly crest region of Calcutta during the equinoxes and Joshi et al. (2019) found that scintillation variability in the autumnal equinox was highly correlated with the periodic geomagnetic activity. Sahithi et al (2019) investigated the climatology of scintillations over India at stations located around the crest and trough regions of the EIA, identifying that the probability of scintillations is higher during March equinox and December solstice, and lowest during June solstice, maximizing in the post-sunset hours.

In the South-East Asian sector, a climatological analysis from 1 March to 9 October 2015 is reported by Povero et al. (2017), in which the scintillation occurrence is evaluated by grouping the dataset into quiet and disturbed conditions, sorted according Dst and local Kp index derived by a network of magnetometers. This allowed to identify the scintillation inhibition and/or enhancement that may follow a geomagnetic storm and that is due to the interplay of the prompt penetration electric fields (PPEF)

(Wei et al., 2015) and the disturbance dynamo electric fields (DDEF) (Yamazaki and Maute, 2017), affecting the low-latitude electrodynamics. Lan et al. (2017) reports a climatological analysis of the scintillation occurrence over Vietnam for the period 2006–2014. Also, in this longitudinal sector, the scintillation activity is maximum during equinox months for all the years and has a clear dependence on the solar flux.

In Australia, Liu et al. (2017) analyzed GNSS LoL events by ionospheric scintillation from 2011 to 2015, which were correlated with solar activity, and increased during equinox months.

In this work, we investigate the amplitude scintillation at SA sector during the full solar cycle 24, using S_4 index, in order to understand its behavior over a region affected by large probability of small-scale irregularities formation due to the presence of the crests of the EIA and at the SAMA, for magnetic latitudes lower than 40º.

The challenges posed by the low-latitude electrodynamics to the ionospheric scintillation modelling and forecasting are due to the random-like behavior of the day-to-day formation of EPBs (Balan et al., 2018; Li et al., 2020), and to the interplay between PPEF and DDEF during storm-time (Li et al., 2020). A schematic view of the coupled processes ruling out the EPB formation and its short-term variability can be found in Fig. 1 of Abdu (2019). Understanding how the scintillation behaves in different periods of solar cycle, as well as at different locations, can be a useful tool to support the forecasting of the GNSS signal degradation probability, the prediction of when and where the tracking obstruction is likely to occur and the development of mitigation techniques able to ensure the accuracy of navigation systems, even under disturbed ionospheric conditions.

This paper is organized in 3 sections. In Section 2, we provide detail about the network of GPS receivers we selected for this study, together with the data provided and their methods of analysis. In Section 3, we provide the results in different perspectives and their analysis. In Section 4 we provide the conclusions.

Data and Method

In this work, we characterize the amplitude scintillation at the SA sector during the solar cycle 24 (from 2009 to 2019), using the GPS stations of the Low-Latitude Ionospheric Sensor Network (LISN), taking into account the data availability for each year, and the dip angles of the stations' locations. The dip angles are the magnetic field lines angles made with the horizontal plane and the values were considered here for January 2015. Here we considered the GPS constellation and used the ground stations listed in Table 1, which gives their geographic positions and dip angles. The stations are separated in three main regions over SA: north and south of the magnetic equator, i.e., in correspondence with the expected position of the EIA crests, and at the magnetic equator, i.e., in correspondence with the ionospheric trough.

Table 1 - GPS Stations: Names and positions of GPS stations, ordered by dip angles: 1- north of magnetic equator; 2: at the magnetic equator; 3: south of magnetic equator.

	Station name	**Short name**	**Latitude**	**Longitude**	**Dip angle**
1	Bogota	BOG	04.0N	074.0W	27.4N
	Boa Vista	BOA	02.8N	060.7W	18.6N
	Iquitos	IQT	03.7S	073.3W	14.4N
	Piura	PIU	05.2S	080.6W	12.5N
2	Santarem	SAN	02.4S	054.7W	03.8N
	Rio Branco	RBR	10.0S	067.9W	01.2N
	Huancayo	HUA	12.0S	075.3W	00.3S
	Puerto Maldonado	PMD	12.6S	069.2W	02.9S
3	Sao Luis	SLU	02.6S	044.2W	08.8S
	Tacna	TAC	18.0S	070.2W	12.1S
	Potosi	POT	19.6S	065.8W	16.5S
	Cuiaba	CUI	15.6S	056.1W	17.5S
	Antofagasta	ANT	23.7S	070.4W	21.3S
	Petrolina	PET	09.3S	040.5W	24.7S
	Natal	NAT	05.8S	035.2W	24.9S
	Dourados	DOU	22.2S	054.9W	28.1S
	Casleo	LEO	31.8S	069.3W	32.4S
	Santa Maria	SMA	29.7S	053.7W	37.4S
	Cachoeira Paulista	CAC	22.7S	045.0W	37.5S
	Villegas	VIL	35.0S	063.0W	37.5S

These stations' locations and the magnetic equator for the year 2015 are shown in Figure 1, where the circles represent the regions around the stations where the satellites can be tracked, for elevation angles above 30°. Due to the data availability, some stations (within green circles) are included to fill gaps of others with similar dip angles. The opacity of the circles increases with the percentage of data availability during the solar cycle 24. The selection of such stations allows having a homogenous dataset with comparable statistics in each of the considered years. The station SAN is considered only in 2013 to fill the gap of RBR; POT is considered from 2015 to 2019 to fill the gap of CUI; ANT is considered from 2009 to 2011 and PET from 2017 to 2019 to fill the gap of NAT; and SMA is considered from 2011 to 2012 and CAC in 2013 to fill the gap of VIL.

The amplitude scintillation index (S_4) is the standard deviation of the signal intensity normalized to the intensity averaged over 60s (Fremouw et al, 1978; Guo et al., 2019) and is given by the Eq. (1).

$$S_4 = \sqrt{\frac{<P_{det}^2> - <P_{det}>^2}{<P_{det}>^2}} \tag{1}$$

where P_{det} is the detrending signal measurement and < > represents the mathematical average over 60s. To detrend the noise created by low-frequency signal intensity variation, such as variation caused by the satellite movement, the signal intensity measurements, P, is passed first through a low-pass filter to obtain the intensity trend, P_{trend}, and then P is normalized by 60s averaged outputs of the filter (Van Dierendonck et al, 1993; Van Dierendonck and Arbesser-Rastburg, 2004) according to the Eq. (2).

$$P_{det} = \frac{P}{<P_{trend}>_{60s}} \tag{2}$$

To minimize errors due to signal multipath caused by surface terrains and human-made structures that may mimic amplitude scintillation (e.g., D'Angelo et al., 2015), we excluded data from satellites with low elevation angles by setting a cutoff angle of 30º. This filter was applied to all stations and periods of time considered. Then, we verticalized these indexes to consider the geometric effects at different elevation angles according to Eq. (3).

$$S_4^{vert} = \frac{S_4^{slant}}{(F(\alpha_{elev}))^b} \tag{3}$$

where S_4^{slant} is the index provided by LISN at a given elevation angle along the slant path; $F(\alpha_{elev})$ is the obliquity factor; and the exponent b, which depends on ionospheric conditions, is assumed to be 0.9. The changes of b do not interfere meaningfully in the results of the present work. Such discussion has already been made by Spogli et al. (2009) and Alfonsi et al. (2011). The obliquity factor is defined by Eq. (4).

$$F(\alpha_{elev}) = \sqrt{\frac{1}{1-(\frac{R_E cos\alpha_{elev}}{R_E+H_{IPP}})^2}} \tag{4}$$

where R_E is the Earth radius, 6370 km, and H_{IPP} is the height of the Ionospheric Piercing Point (IPP), which is assumed to be 350 km (Mannucci et al., 1993). While projecting, two assumptions are implicit: the single ionospheric layer approximation and the weak scintillation regime. A critical discussion about the adoption of a climatological picture based on the use of vertical indices can be found in Spogli et al. (2013a) and in De Franceschi et al., (2019). We remind that the approximation lying below the verticalization process may lead to an underestimation of the scintillation occurrence, affecting mainly the values close to the threshold to calculate occurrence (De Franceschi et al., 2019). In the remainder of the paper, we refer to S_4^{vert} as S_4.

The data provided by LISN is divided by GPS stations, and for each station the S_4 index is given for every minute by each satellite (around 10-12 satellites). After applying the cutoff angle of 30° and calculating the verticalized index, the new data is divided by integral numbers of dip angles intervals, from 40 to -40 degrees (North to South) and by each day of the year. This means that a dip angle interval may have data from more than one GPS station (see Figure 1).

Results

This work is divided into 3 topics. The first topic presents the results of the full solar cycle 24 at the SA sector, from 2009 to 2019, with the aim to understand the agreement between the solar activity and the scintillation, and also the locations and seasons of greater scintillation occurrences. The second topic presents the daily variation of scintillation showing the periods of time when their occurrence prevails. The third topic includes the ionospheric scintillation activity when specific geomagnetic storms occur during daytime.

Full characterization of solar cycle 24.

Figure 2 shows the results of a higher-level characterization of the amplitude scintillation during solar cycle 24, divided by year (2009 to 2019). The percentage of times that S_4 index surpassed the value of 0.2 is calculated by each day and each dip angle with the percentage of occurrence identified by different colors in Figure 2. The threshold of 0.2 is able to identify scintillation regimes from moderate to strong. Because $S_4 > 0.2$ higher than 20% was very rare in the solar cycle 24 (only 4 cases were found in the solar maximum), we specify here 20% as the maximum percentage in the plots.

Solar activity and scintillation occurrences in Figure 2 are clearly associated, as expected. The solar cycle 24 starts in 2009 with very low occurrence of scintillation, and as the solar activity increases, the percentages of occurrence also increase, reaching a peak in 2014. After 2014, the scintillation occurrences gradually decrease as the solar activity decreases until 2019, which is the end of solar cycle 24. This is confirmed by Figure 3, which shows the progression of the full solar cycle 24, from 2009 to 2019. Figure 3 compares the monthly smoothed sunspot number, the R12 ionospheric index, provided by Space Weather Prediction Center (SWPC) / National Oceanic and Atmospheric Administration (NOAA), with the monthly percentage of S_4 index over 0.2, showing a similarity between the 2 graphs. Figure 3 also depicts how the scintillation occurrence well fit with the double peak structure with maxima in years

2012 and 2014/2015 that featured the sunspot number behavior. The close association of solar activity and scintillation agrees with some previous results, such as provided by Muella et al. (2017) over a station located in correspondence with the expected position of the southern crest of EIA at SA sector from 1997 to 2014; by Lan et al. (2017) over 3 stations located at the North of magnetic equator in Vietnam from 2006 to 2014; and by Li et al. (2020) over the low-latitude station of Sanya (China) from 2004 to 2019. The dependence on solar activity for scintillation is confirmed by our results over a wider geographic area and during the full solar cycle 24.

Figure 2 also shows the impact of EIA on the scintillation. Near the magnetic equator, where the magnetic latitudes are lower than ±10º, the scintillation occurrences are scarce. This is the region where the ExB drift is maximum and, by consequence, the F-layer ionospheric plasma undergoes the uplift during the daytime. In the regions centered at ±20º, the scintillation is more frequent. These regions are in correspondence with the expected position of the crests of EIA, that are due to the plasma accumulation formed mainly by the removal of plasma around the magnetic equator due to the ExB itself (Balan et al., 2018). In the post-sunset hours, the more probable seed to EPBs is the pre-reversal enhancement (PRE) of the eastward electric field, and there is a consequent intensification of the crests of the ExB drift, creating favorable conditions for the growth of Rayleigh-Taylor instabilities (Spogli et al., 2016; Sripathi et al., 2018; Li et al., 2020). There is an asymmetry between northern and southern crests of the EIA, resulting in more frequent scintillations and with larger S_4 occurrence, most likely attributed to the SAMA, where particles from the inner Van Allen radiation belt precipitate into the atmosphere, due to the week geomagnetic field over the region (Abdu et al., 2005). The impact of EIA, associated with EPBs, and SAMA, associated with particle's precipitation, on the scintillation agrees with previous investigations, such as Spogli et al. (2013a) in 2011 over Latin America and Antarctica, and Spogli et al. (2013b) in 2011 over Brazil. At latitudes higher than ±30º, the scintillations are rare, which agrees with studies such as Brahmanandam et al. (2012) and Juan et al. (2018).

Another noteworthy aspect shown in Figure 2 is that, under high solar flux conditions, scintillation appears around September equinox, which is spring in most part of SA, increases even more in the December solstice, summer in SA, and continues all the way to March equinox, autumn in SA. Although, the stations we selected are divided between North and South of magnetic equator, most of them are located at the southern hemisphere or near the geographic equator, where the sun is at the zenith during summer solstice and equinoxes, respectively. Figure 3 also confirms the increase of scintillations between September and March. During the winter, the scintillations are almost absent, confirming previous works, such as Alfonsi at el. (2013) from 2010 to 2011 at the southern crest of EIA, Cesaroni et al. (2015) in 2015 over Brazil, Muella et al. (2017) from 1997 to 2014 at the southern crest of EIA, Brahmanandam et al. (2012) in 2008 at low latitudes using satellites, Sahithi et al (2019) over the Indian sub-continent, Lan et al. (2017) from 2006 to 2014 over Vietnam, Li et al. (2020) from 2004 to 2019 over Sanya (Southern China), and Liu et al. (2017) from 2011 to 2015 over Australia.

Daily variation during solar maximum.

A different perspective is shown in Figure 4, which shows the daily variation in Universal Time (UT) of scintillation for the years of solar maximum (2012-2014) at 4 different locations: PIU at the north of magnetic equator (dip~15°N), HUA at the magnetic equator (dip~0°N), TAC, CUI at the south of magnetic equator (dip~15°S) and NAT at the south, even further from magnetic equator (dip~25°S). The station TAC is included to cover the CUI lack of data in 2014. The sunrise (blue lines) and sunset (red lines) are also included, considering the time at IPP, so the sunrises are earlier, and sunset are later than they would be on the surface of Earth. For each plot, the time advances from the bottom (0h) to the top (24h) and from left (January) to right (December). The bin size is 6 minutes x 1 day and the color bars represent the percentage of $S_4 > 0.2$ and it is found to peak up to 60%.

Figure 4 shows that the scintillation occurs in the post-sunset hours in all cases, starting just after the sunset and ending few hours before the sunrise. Few rare cases of daytime scintillation can also be found, that are thought to be due to E-layer irregularities (e.g., Alfonsi et al., 2013 and references therein). As in Figure 2, here the scintillation also happens in the spring and summer months of the southern hemisphere. The presence of EIA is evidenced by the higher occurrences at the northern and southern crests and lower occurrences at the magnetic equator. And the asymmetry between both crests is clear here, seen by a higher number of occurrences of $S_4 > 0.2$ in the southern crest and by the time that the scintillation ends, which is closer to sunrise, compared with the northern crest. This can be an evidence of particle's precipitation due to the SAMA adding to EPB's formation at the southern crest. The presence of post-midnight scintillations is also important and reflects the presence of post-midnight EPBs that are of 2 kinds: (i) long-living EPBs generated at post-sunset hours and migrating in the field of view of the receiver and (ii) freshly generated EPBs. The results presented here agree with results from previous investigations, such as Spogli et al. (2013a), Spogli et al. (2013b), and Bougard et al. (2013) over SA, Tilahun (2020) over Africa, Sahithi et al (2019) over Indian sub-continent, and Li et al. (2020) over Southern China.

Effect of a geomagnetic storm

To illustrate how a geomagnetic storm can affect the formation of EPBs and the consequent scintillation patterns recorded on L-band signals, and how this can pose a serious challenge to the climatology-based modelling, we present here 2 case studies during a storm that occurred during October/November 2012 (Matsui et al., 2016) and March 2015 (equinoxes, near solar maximum). The latter is the well-known 2015 St. Patrick's Day storm, that has been widely studied in the recent literature (e.g., Tulasi Ram et al., 2016; Spogli et al., 2016; Kil et al., 2016; Venkatesh et al., 2017; Dmitriev et al., 2017). Figure 5 shows 1-minute resolution plots of auroral electrojet (*AE*), *Bz* component of the interplanetary magnetic field (*IMF-Bz*), horizontal component of the symmetric disturbance index (*SYM-H*) the S_4 index of 2 stations, NAT and DOU, and the disturbance to the equatorial ionospheric eastward electric field (Δ*EEF*) estimated at the local time of these stations. The *AE* and *IMF-Bz* indexes were provided by the World Data Center for Geomagnetism, at Kyoto University, the *SYM-H* index, by the Omniweb data portal, and the disturbance to the *EEF* (Δ*EEF*), modelled by the Cooperative Institute for Research in Environmental Sciences (CIRES) at the University of Colorado Boulder. Δ*EEF* is derived by the application of a digital filter that allows mapping the interplanetary electric field (IEF) retrieved from Advanced Composition Explorer (ACE) satellite data through a transfer function model (Manoj et al., 2008; Manoj & Maus, 2012). Such kind of approach to model EEF disturbance, supported by *IMF-Bz*, has been proven to be effective in enabling investigation of the role of PPEFs in the storm-time behavior of the Equatorial Electrojet (EEJ) (e.g., Spogli et al., 2020, Alfonsi et al., 2021). Moreover, *AE* is here used to speculate about the behavior of Joule and particle heating possibly leading to storm-time neutral winds triggering DDEFs (Yamazaki and Maute, 2017)

According to Figure 5, the *IMF-Bz* component was flipping between positive and negative values until 05:32 UT on 01 November, remaining negative from this time until 01:08 UT on 02 November. This condition caused a geomagnetic storm with a sudden commencement at 15:40 UT on 31 October 2012, and minimum *SYM-H* value of -68nT at 20:01 UT on 01 November. The *AE* reached the expressive value of 1912 nT at 15:16 UT on 01 November. The post-sunset scintillation at NAT was inhibited on 01 November and at CUI, on 31 October and 01 November. According to the empirical rule, known as "Aaron criteria", when the disturbance occurs in the afternoon, before PRE, there is an inhibition of irregularities (Aarons, 1991; Li et al., 2008; Spogli et al., 2016; Sripathi et al., 2018), which explains the scintillation inhibition in the post-sunset on 01 November at both stations. In this case, the long-lasting negative *IMF-Bz* condition, under which no PPEF event occur, and the large values of *AE*, triggered a significant Joule/particle heating at high-latitude, resulting in DDEF events. This leads to a significant lowering of the EEJ intensity before the sunset, inhibiting the conditions for the PRE. This confirms previous investigations, such as Povero et al. (2017). Due to the longitudinal difference between NAT and CUI stations, the Δ*EEF* behaviors were different. The negative Δ*EEF* was higher at CUI (~-1.2) compared with at NAT (~-0.6) just before the post-sunset scintillation peak of 01 November, and stayed a longer time in negative values, which leads to a possible explanation for the scintillation suppression at CUI.

Figure 6 shows the second case study for the 2015 St. Patrick's Day storm, when the sudden commencement of the geomagnetic storm happened at 04:46 UT on 17 March, seen by the raise of *SYM-H* and a positive *IMF-Bz*. The *IMF-Bz* turned negative at 06:05 UT on 17 March causing a decrease of *SYM-H* after 06:22 UT on 17 March, which represented the onset of the main phase of the storm. The *IMF-Bz* flipped between positive and negative values until 11:49 UT on 17 March, when it remained negative for more than 12 hours, until 23:51 UT on 17 March, resulting in a *SYM-H* minimum of -232 nT at 23:05 UT on 17 March. Meanwhile, the AE presented several peaks, with highest value of 2298 nT at 13:58 UT on 17 March. At NAT and DOU stations, the post-sunset scintillation inhibitions happened in 17 and 18 March, and the ΔEEF reached -1.08 mV/m at 06:40 UT on 17 March at NAT and -1.32 mV/m at the same time at DOU. In this case, the higher values of *AE*, the long-lasting negative values of *IMF-Bz*, the high negative values of *SYM-H* and ΔEEF at both stations started before the sunset on 17 March at both stations. The St. Patrick's Day storm triggered two strong PPEF events (Venkatesh et al., 2017), visible from the ΔEEF time profile. The largely varying conditions of the *IMF-Bz*, which resulted in various positive and negative disturbances on the EFF, occurs mainly in the local daytime, likely indicating that the PPEF events have no influence on the possible seeding to EPBs in the proximity of sunset hours. Conversely, the DDEF, whose presence is indicated by the increase if the AE index delayed of few hours, are active during the post sunset hours and are effective in inhibiting the conditions for the PRE, resulting in an inhibition of the scintillation activity at both sites. The auroral activity lasted all over the recovery phase of the storm, resulting into conditions favoring the inhibition of the EPB seeding triggered by DDEF events. As a consequence, the inhibition of scintillation also happened at both station on 17 and 18 March.

The climatology base model during solar cycle 24 over SA presents important behaviors of the scintillations, including the agreement with solar activity, the locations of occurrences and lack of occurrences, and the variability due to seasonality and period of time during the day. This model, however, is limited by the actual ionospheric weather, impacted by different features of geomagnetic storms, which makes necessary to analyze each storm separately.

Conclusions

Scintillations affect radio signals, such as GNSS, that propagate through the ionosphere, and are caused by ionospheric irregularities that have a typical scale size below the Fresnel's scale for that specific geometry of observation and wavelength (hundreds of meters for GNSS signals received at ground). The amplitude scintillation occurrence was analyzed in this work by investigating the S_4 index for the solar cycle 24 at SA sector and magnetic latitudes lower than 40º. The main drivers to this occurrence are the small-scale irregularities that form mainly (but not only) in the post-sunset hours and that are embedded in EPBs.

The results show that the scintillation increases according to the solar activity, attaining higher values during solar maximum, when the ionization density increases at the F-region and the irregularities occur in a background of enhanced ionization density (Basu et al., 2002, Abdu, 2019). This is valid for all latitudes in the considered sector. On the other hand, during solar minimum, the ionization density is reduced and the scintillation decreases. This confirms also the close relationships between the occurrence of EPBs and EEJ strength, that is modulated by the solar flux and the season (e.g., Dabas et al., 2003).

The scintillation is of lower intensity at magnetic equator and higher intensity at low latitudes near the northern and southern crests of EIA, in the regions around ±20º. They are more pronounced during spring and summer seasons of solar maximum, after sunset, suggesting a strong effect of EPBs.

In the southern crest the scintillations are more pronounced and frequent and this ionization asymmetry might be due to the presence of SAMA anomaly over that region, where the precipitation of particles is added to the formation of EPBs.

The scintillations start after sunset and end few hours before sunrise, despite some very rare daytime scintillation events can occur. And the plots of Figure 4 confirm their enhancement during spring and summer, and also the asymmetry between the northern and southern crests of EIA.

The climatology base model that we present in this paper is challenged when geomagnetic storm conditions are present and may vary according to the specific features of the storms.

Declarations

Ethics approval and consent to participate

Not applicable

Consent for publication

Not applicable

List of abbreviations

ACE: Advanced Composition Explorer

AE: Auroral Electrojet

CIRES: Cooperative Institute for Research in Environmental Sciences

DDEF: Disturbance Dynamo Electric Field

EEF: Equatorial Ionospheric Eastward Electric Field

EEJ: Equatorial Electrojet

EIA: Equatorial Ionospheric Anomaly

EPB: Equatorial Plasma Bubbles

F3C: FORMOSAT-3/COSMIC

GBSC: Ground-Based Scintillation Climatology

GMSS: Global Navigation Satellite System

GPS: Global Positioning System

HF: High Frequency

IEF: Interplanetary Electric Field

IGRF: International Geomagnetic Reference Field

IMF: Interplanetary Magnetic Field

IPP: Ionospheric Piercing Point

LISN: Low-Latitude Ionospheric Sensor Network

LoL: Loss of signal Lock

LT: Local Time

NOAA: National Oceanic and Atmospheric Administration

PPEF: Prompt Penetration Electric Field

PRE: Pre-Reversal Enhancement

SA: South American

SAMA: South Atlantic Magnetic Anomaly

SWPC: Space Weather Prediction Center

SYM: Symmetric Disturbance Index

TEC: Total Electron Content

UT: Universal Time

Availability of data and materials

The datasets generated and/or analyzed during the current study are available in the following repositories: LISN at http://lisn.igp.gob.pe; SWPC/NOAA at http://swpc.noaa.gov; World Data Center for Geomagnetism at http://wdc.kugi.kyoto-u.ac.jp; Omniweb data portal at https://omniweb.gsfc.nasa.gov; CIRES at https://www.geomag.us/index.html.

Competing interests

The authors declare that they have no competing interests.

Funding

EPM thanks Coordenação de Aperfeiçoamento de Pessoal de Nível Superior Brasil (CAPES) for the financial support providing scholarship through Financial Code 001; EC thanks the National Council for Scientific and Technological Development - CNPq (process no: 303299/2016-9) and São Paulo Research Foundation – FAPESP (process no: 2019/05455-2) for individual research support. MTAHM acknowledges support from CNPq through grant 314261/2020-6.

Authors' contributions

All authors were involved with this work. EPM collect and processed the data, built and run the codes, generate the plots and wrote the manuscript’s draft. EC helped in the data analysis and structured the manuscript; LS helped in the data analysis and improved the manuscript; MTAHM helped in the data analysis and performed corrections in the manuscript. All authors read and approved the final manuscript.

Acknowledgements

We thank LISN , SWPC/NOAA, World Data Center for Geomagnetism at Kyoto University, Omniweb data portal and CIRES at the University of Colorado Boulder for the easy access to their data.

References

Aarons J (1991) The role of the ring current in the generation or inhibition of equatorial F layer irregularities during magnetic storms. Radio Science. 26 (4). 1131-1149.

Abdu MA, Batista IS, Carrasco AJ, Brum CGM (2005) South Atlantic magnetic anomaly ionization: A review and a new focus on electrodynamic effects in the equatorial ionosphere. Journal of Atmospheric and Solar-Terrestrial Physics. 67:1643-1657. doi: 10.1016/j.jastp.2005.01.014.

Abdu MA (2019) Day-to-day and short-term variabilities in the equatorial plasma bubble/spread F irregularity seeding and development. Progress in Earth and Planetary Science. 6(1). doi: 10.1186/s40645-019-0258-1.

Akala AO, Amaeshi LLN, Somoye EO, Idolor RO, Okoro E, Doherty PH, Groves K, Carrano C, Bridgwood CT, Baki P, D'ujanga FM, Seemala GK, Akala BAO (2015) Climatology of GPS amplitude scintillations over equatorial Africa during the minimum and ascending phases of solar cycle 24. Astrophysics and Space Science. 357(1):17. doi: 10.1007/s10509-015-2292-9.

Alfonsi L, Spogli L, De Franceschi G, Romano V, Aquino M, Dodson A (2011) Bipolar climatology of GPS ionospheric scintillation at solar minimum. Radio Science. 46(3). doi: 10.1029/2010RS004571.

Alfonsi L, Spogli L, Pezzopane M, Romano V, Zuccheretti E, De Franceschi G, Cabrera MA, Ezquer RG (2013) Comparative analysis of spread-F signature and GPS scintillation occurrences at Tucumán, Argentina. Journal of Geophysical Research: Space Physics. 118:4483-4502. doi: 10.1002/jgra.50378.

Alfonsi L, Cesaroni C, Spogli L, Regi M, Paul A, Ray S, Lepidi S, Di Mauro D, Haralambous H, Oikonomou C, Shreedevi PR, Sinha AK (2021) Ionospheric disturbances over the Indian sector during 8 September 2017 geomagnetic storm: plasma structuring and propagation. Space Weather. e2020SW002607. doi: 10.1029/2020SW002607.

Balan N, Liu L, Le H (2018) A brief review of equatorial ionization anomaly and ionospheric irregularities. Earth and Planetary Physics. 2:1-19. doi: 10.26464/epp2018025.

Basu S, Groves KM, Basu Su, Sultan PJ (2002) Specification and forecasting of scintillations in communication navigation links: current status and future plans. Journal of Atmospheric and Solar-Terrestrial Physics. 64:1745-1754. doi: 10.1016/S1364-6826(02)00124-4.

Bougard B, Simsky A, Sleewaegen JM, Park J, Aquino M, Spogli L, Romano V, Mendonca MAM, Monico JFG (2013) CALIBRA: mitigating the impact of ionospheric scintillation on precise point positioning in Brazil. In 7th GNSS vulnerabilities and solutions conference, April, 2013.

Brahmanandam PS, Uma G, Liu JY, Chu YH, Devi NSMPL, Kakinami Y (2012) Global S4 index variations observed using FORMOSAT-3/COSMIC GPS RO technique during a solar minimum year. Journal of Geophysical Research: Space Physics. 117(A9). doi: 10.1029/2012JA017966.

Cesaroni C, Spogli L, Alfonsi L, De Franceschi G, Ciraolo L, Francisco J, Monico JFG, Scotto C, Romano V, Aquino M, Bougard B (2015) L-band scintillations and calibrated total electron content gradients over Brazil during the last solar maximum. Journal of Space Weather and Space Climate. 5:A36. doi: 10.1051/swsc/2015038.

Conker RS, El-Arini MB, Hegarty CJ, Hsiao T (2003) Modeling the effects of ionospheric scintillation on GPS/Satellite-Based Augmentation System availability. Radio Science. 38:1001. doi: 10.1029/2000RS002604.

Correia E, Muella MTAH, Lucilla A, Prol FS, Camargo POC (2018) GPS Scintillations and Total Electron Content Climatology in the Southern American Sector. In: Dr. Dogan Ugur Sanli. (Org.). Accuracy of GNSS Methods. 1ed. London: IntechOpen, 1:47-70. doi: 10.5772/intechopen.79218.

D'Angelo G, Spogli L, Cesaroni C, Sgrigna V, Alfonsi L, Aquino MHO (2015) GNSS data filtering optimization for ionospheric observation. Advances in Space Research. 56(11):2552-2562. doi: 10.1016/j.asr.2015.10.002.

Dabas RS, Singh L, Lakshmi DR, Subramanyam P, Chopra P, Garg SC (2003) Evolution and dynamics of equatorial plasma bubbles: Relationships to ExB drift, postsunset total electron content enhancements, and equatorial electrojet strength. Radio Science. 38(4). doi: 10.1029/2001RS002586.

Damaceno JG, Bolmgren K, Bruno J, De Franceschi G, Mitchell C, Cafaro M (2020) GPS loss of lock statistics over Brazil during the 24th solar cycle. Advances in Space Research. 66(2):219-225. doi: 10.1016/j.asr.2020.03.041.

De Franceschi G, Spogli L, Alfonsi L, Romano V, Cesaroni C, Hunstad I (2019) The ionospheric irregularities climatology over Svalbard from solar cycle 23. Scientific reports. 9(1):1-14. doi: 10.1038/s41598-019-44829-5.

De Paula ER, Oliveira CBA, Caton RG, Negreti PM, Batista IS, Martinon ARF, Neto AC, Abdu MA, Monico JFG, Sousasantos J, Moraes AO (2019) Ionospheric irregularity behavior during the September 6–10, 2017 magnetic storm over Brazilian equatorial–low latitudes. Earth, Planets and Space. 71(42). doi: 10.1186/s40623-019-1020-z.

De Rezende LFC, De Paula ER, Kantor IJ, Kintner PM (2007) Mapping and Survey of Plasma Bubbles over Brazilian Territory. The Journal of Navigation. 60:69-81. doi: 10.1017/S0373463307004006.

De Rezende LFC, De Paula E, Stephany S, Kantor IJ, Muella MTAH, Siqueira PM, Correa KS (2010) Survey and prediction of the ionospheric scintillation using data mining techniques. Space Weather. 8(6):S06D09. doi: 10.1029/2009SW000532.

Dmitriev AV, Suvorova AV, Klimenko MV, Klimenko VV, Ratovsky KG, Rakhmatulin RA, Parkhomov VA (2017) Predictable and unpredictable ionospheric disturbances during St. Patrick's Day magnetic storms of 2013 and 2015 and on 8–9 March 2008. Journal of Geophysical Research: Space Physics. 122(2):2398-2423. doi: 10.1002/2016JA023260.

Fremouw EJ, Leadabrand RL, Livingston RC, Cousins MD, Rino CL, Fair BC, Long RA (1978) Early results from the DNA Wideband satellite experiment—Complex-signal scintillation. Radio Sci. 13(1):167–187. doi: 10.1029/RS013i001p00167.

Ghobadi H, Spogli L, Alfonsi L, Cesaroni C, Cicone A, Linty N, Romano V, Cafaro M (2020) Disentangling ionospheric refraction and diffraction effects in GNSS raw phase through fast iterative filtering technique. GPS Solutions. 24(3):1-13, doi: 10.1007/s10291-020-01001-1.

Goswami S, Paul KS, Paul A (2017) Assessment of GPS Multifrequency Signal Characteristics During Periods of Ionospheric Scintillations from an Anomaly Crest Location. Radio Science. 52(9):1214-1222. doi: 10.1002/2017RS006295.

Guo K, Aquino M, Veetil SV (2019) Ionospheric scintillation intensity fading characteristics and GPS receiver tracking performance at low latitudes. GPS Solutions. 23-43. doi: 10.1007/s10291-019-0835-1.

Joshi LM, Tsai LC, Su SY, Caton RG, Groves KM, Lu, CH (2019) On the Nature of the Intraseasonal Variability of Nighttime Ionospheric Irregularities Over Taiwan. Journal of Geophysical Research: Space Physics. 124(5):3609-3622. doi: 10.1029/2018JA026419.

Juan JM, Sanz J, Gonzalez-Casado G, Garcia AR, Camps A, Riba J, Barbosa J, Blanch E, Altadill D, Pérez RO (2018) Feasibility of precise navigation in high and low latitude regions under scintillation conditions. Journal of Space Weather and Space Climate. 8(A05). doi: 10.1051/swsc/2017047.

Khadka SM, Valladares C, Pradipta R, Pacheco E, Condor P (2016) On the mutual relationship of the equatorial electrojet, TEC and scintillation in the Peruvian sector. Radio Science. 51(6):742-751. doi: 10.1002/2016RS005966.

Kil H, Lee WK, Paxton LJ, Hairston MR, Jee G (2016) Equatorial broad plasma depletions associated with the evening prereversal enhancement and plasma bubbles during the 17 March 2015 storm. Journal of Geophysical Research: Space Physics. 121(10):10-209. doi: 10.1002/2016JA023335.

Kintner PM, Humphreys T, Hinks J (2009) GNSS and Ionospheric Scintillation – How to survive to the next solar maximum. Inside GNSS. 22-30.

Lan TT, Le HM, Amory-Mazaudier C, Fleury R (2017) Climatology of ionospheric scintillation over the Vietnam low-latitude region for the period 2006–2014. Advances in Space Research. 60(8):1657-1669. doi: 10.1016/j.asr.2017.05.005.

Li G, Ning B, Zhao B, Liu L, Liu JY, Yumoto K (2008) Effects of geomagnetic storm on GPS ionospheric scintillations at Sanya. Journal of Atmospheric and Solar-Terrestrial Physics. 70:1034–1045. doi: 10.1016/j.jastp.2008.01.003.

Li G, Ning B, Otsuka Y, Abdu MA, Abadi P, Liu Z, Spogli L, Wan W (2020) Challenges to Equatorial Plasma Bubble and Ionospheric Scintillation Short-Term Forecasting and Future Aspects in East and Southeast Asia. Surveys in Geophysics. 1-38. doi: 10.1007/s10712-020-09613-5.

Liu Y, Fu L, Wang J, Zhang C (2017) Study of GNSS Loss of Lock Characteristics under Ionosphere Scintillation with GNSS Data at Weipa (Australia) During Solar Maximum Phase. Sensors. 17(10):2205. doi: 10.3390/s17102205.

Mannucci AJ, Wilson BD, Edwards CD (1993) A new method for monitoring the Earth ionosphere total electron content using the GPS global network. In Proceedings of the 1993 ION GPS-93, Salt Lake City, UT, USA. 22–24.

Manoj C, Maus S, Lühr H, Alken P 92008) Penetration characteristics of the interplanetary electric field to the daytime equatorial ionosphere. Journal of Geophysical Research: Space Physics. 113(A12). doi: 10.1029/2008JA013381.

Manoj C, Maus S (2012) A real - time forecast service for the ionospheric equatorial zonal electric field. Space Weather. 10(9). doi: 10.1029/2012SW000825.

Matsui H, Paulson KW, Torbert RB, Spence HE, Kletzing CA, Kurth WS, Skoug RM, Larsen BA, Breneman AW (2016) Nonlinearity in chorus waves during a geomagnetic storm on 1 November 2012. Journal of Geophysical Research: Space Physics. 121(1):358-373. doi: 10.1002/2015JA021772.

Moro J, Denardini CM, Abdu MA, Correia E, Schuch NJ, Makita K (2012) Latitudinal dependence of cosmic noise absorption in the ionosphere over the SAMA region during the September 2008 magnetic storm. Journal of Geophysical Research. 117:A06331-1-7. doi: 10.1029/2011JA017405.

Muella MTAH, Duarte-Silva MH, Moraes AO, De Paula ER, De Rezende LFC, Alfonsi L, Affonso BJ (2017) Climatology and modeling of ionospheric scintillations and irregularity zonal drifts at the equatorial anomaly crest region. Annales Geophysicae. 35:1201-1218. doi: 10.5194/angeo-35-1201-2017.

Oliveira CBA, Espejo TMS, Moraes A, Costa E, Sousasantos J, Lourenco LFD, Abdu, MA (2020) Analysis of Plasma Bubble Signatures in Total Electron Content Maps of the Low-Latitude Ionosphere: A Simplified Methodology. Surveys in Geophysics. 41:897–931. doi: 10.1007/s10712-020-09584-7.

Olwendo J, Cilliers P (2018) A comparison of ionospheric scintillation proxy indices derived from low rate IGS data with the amplitude scintillation index, S4, in a low latitude region over Africa. Journal of Atmospheric and Solar-Terrestrial Physics. 173:160-167. doi: 10.1016/j.jastp.2018.04.012.

Povero G, Alfonsi L, Spogli L, Di Mauro D, Cesaroni C, Dovis F, Romero R, Abadi P, Huy ML, The VL, Floury N (2017) Ionosphere monitoring in South East Asia in the ERICA study. Navigation: Journal of The Institute of Navigation. 64(2):273-287. doi: 10.1002/navi.194.

Sahithi K, Sridhar M, Kotamraju SK, Kavya KCS, Sivavaraprasad G, Ratnam DV, Deepthi C (2019) Characteristics of ionospheric scintillation climatology over Indian low-latitude region during the 24th solar maximum period. Geodesy and Geodynamics. 10(2):110-117. doi: 10.1016/j.geog.2018.11.006.

Spogli L, Alfonsi L, De Franceschi G, Romano V, Aquino M, Dodson A (2009) Climatology of GPS ionospheric scintillations over high and mid-latitude European regions. Annales Geophysicae. 27:3429-3437. doi: 10.5194/angeo-27-3429-2009.

Spogli L, Alfonsi L, Cilliers PJ, Correia E, De Franceschi G, Mitchell CN, Romano V, Kinrade J, Cabrera MA (2013a) GPS scintillations and total electron content climatology in the southern low, middle and high latitude regions. Annals of Geophysics. 56:R0220. doi: 10.4401/ag-6240.

Spogli L, Alfonsi L, Romano V, De Franceschi G, Monico JFG, Shimabukuro MH, Bougard B, Aquino M (2013b) Assessing the GNSS scintillation climate over Brazil under increasing solar activity. Journal of Atmospheric and Solar-Terrestrial Physics. 105:199-206. doi: 10.1016/j.jastp.2013.10.003.

Spogli L, Cesaroni C, Mauro DD, Pezzopane M, Alfonsi L, Musico E, Povero G, Pini M, Dovis F, Romero R, Linty N, Abadi P, Nuraeni F, Husin A, Huy ML, Lan TT, La TV, Pillat VG, Floury N (2016) Formation of ionospheric irregularities over Southeast

Asia during the 2015 St. Patrick’s Day storm. Journal of Geophysical Research: Space Physics. 121. doi: 10.1002/2016JA023222.

Spogli L, Sabbagh D, Regi M, Cesaroni C, Perrone L, Alfonsi L, Di Mauro D, Lepidi S, Campuzano SA, Marchetti D, De Santis A, Malagnini A, Scotto C, Cianchini G, Piscini A, Ippolito A (2020) Ionospheric response over Brazil to the August 2018 geomagnetic storm as probed by CSES ‐ 01 and Swarm satellites and by local ground ‐ based observations. Journal of Geophysical Research: Space Physics. e2020JA028368. doi: 10.1029/2020JA028368.

Sreeja VV, Aquino M, Forte B, Elmas Z, Hancock C, De Franceschi G, Alfonsi L, Spogli L. Romano V, Bougard B, Monico JFG, Wernick AW, Sleewaegen JM, Canto A, Da Silva EF (2011) Tackling ionospheric scintillation threat to GNSS in Latin America. Journal of Space Weather and Space Climate. 1:(A5). doi: 10.1051/swsc/2011005.

Sripathi S, Banola S, Emperumal K, Kumar BS, Radicella SM (2018) The role of storm time electrodynamics in suppressing the equatorial plasma bubble development in the recovery phase of a geomagnetic storm. Journal of Geophysical Research: Space Physics. 123:2336–2350. doi: 10.1002/2017JA024956.

Tilahun S (2020) Evening time multi-instrumental verification of ionospheric irregularity in East Africa, Ethiopia. Advances in Space Research. 65(11). doi: 10.1016/j.asr.2020.02.015.

Tulasi Ram S, Yokoyama T, Otsuka Y, Shiokawa K, Sripathi S, Veenadhari B, Heelis R, Ajith KK, Gowtam VS, Gurubaran S, Supnithi P, Le Huy M (2016) Duskside enhancement of equatorial zonal electric field response to convection electric fields during the St. Patrick's Day storm on 17 March 2015. Journal of Geophysical Research: Space Physics. 121(1):538-548. doi: 10.1002/2015JA021932.

Van Dierendonck AJ, Klobuchar J, Hua Q (1993) Ionospheric Scintillation Monitoring Using Commercial Single Frequency C/A Code Receivers. Proceedings of the 6th International Technical Meeting of the Satellite Division of The Institute of Navigation (ION GPS 1993), Salt Lake City, UT. 1333-1342.

Van Dierendonck AJ, Arbesser-Rastburg B (2004) Measuring Ionospheric scintillation in the equatorial region over Africa, including measurements from SBAS geostationary satellite signals. Proceedings of the 17th International Technical Meeting of the Satellite Division of The Institute of Navigation (ION GNSS 2004), Long Beach, CA. 316-324.

Venkatesh K, Tulasi Ram S, Fagundes PR, Seemala GK, Batista IS (2017) Electrodynamic disturbances in the Brazilian equatorial and low ‐ latitude ionosphere on St. Patrick's Day storm of 17 March 2015. Journal of Geophysical Research: Space Physics. 122(4):4553-4570. doi: 10.1002/2017JA024009.

Wei Y, Zhao B, Li G, Wan W (2015) Electric field penetration into Earth' ionosphere: A brief review for 2000–2013. Science Bulletin. 60(8):748–761. doi: 10.1007/s11434-015-0749-4.

Wernik AW, Secan JA, Fremouw EJ (2003) Ionospheric irregularities and scintillation. Advances in Space Research. 31(4):971–981. doi: 10.1016/S0273-1177(02)00795-0.

Yamazaki Y, Maute A (2017) Sq and EEJ—A review on the daily variation of the geomagnetic field caused by ionospheric dynamo currents. Space Science Reviews. 206(1-4):299-405. doi: 10.1007/s11214-016-0282-z.

Yeh KC, Liu CH (1982) Radio wave scintillations in the ionosphere. Proceedings of the IEEE. 70:324-360.

Figure legends

Figure 1 – Map: Map showing the locations of the GPS stations used in this study. The circles represent the area covered by the stations considering an elevation mask of 30° and the dashed orange line refers to the magnetic equator, provided by the International Geomagnetic Reference Field (IGRF-12) model for the year 2015. The opacity of circles increases with the GPS data availability during the solar cycle 24.

Figure **2 – Full characterization:** Occurrence of S_4 index above 0.2 for full solar cycle 24 (2009-2019) as function of magnetic dip angle and month.

Figure 3 – Solar cycle 24: Progression of the solar cycle 24, according to monthly smoothed sunspot number and monthly percentage of S_4 over 0.2.

Figure 4 – Daily variation: Occurrence of S_4 index above 0.2 for solar maximum conditions (2012 to 2014) as a function of the hour of the day (in UT) and of the month. Blue lines indicate the sunrise, while red lines indicate the sunset, both expressed at 350 km.

Figure 5 – Event 2012: *AE*, *IMF-Bz*, *SYM-H*, and S_4 indexes and ΔEEF at NAT and CUI stations, from October 30, 2012 to November 03, 2012. Time in UT.

Figure 6 – Event 2015: Same as Figure 5, from March 15, 2015 to March 19, 2015.

Figures

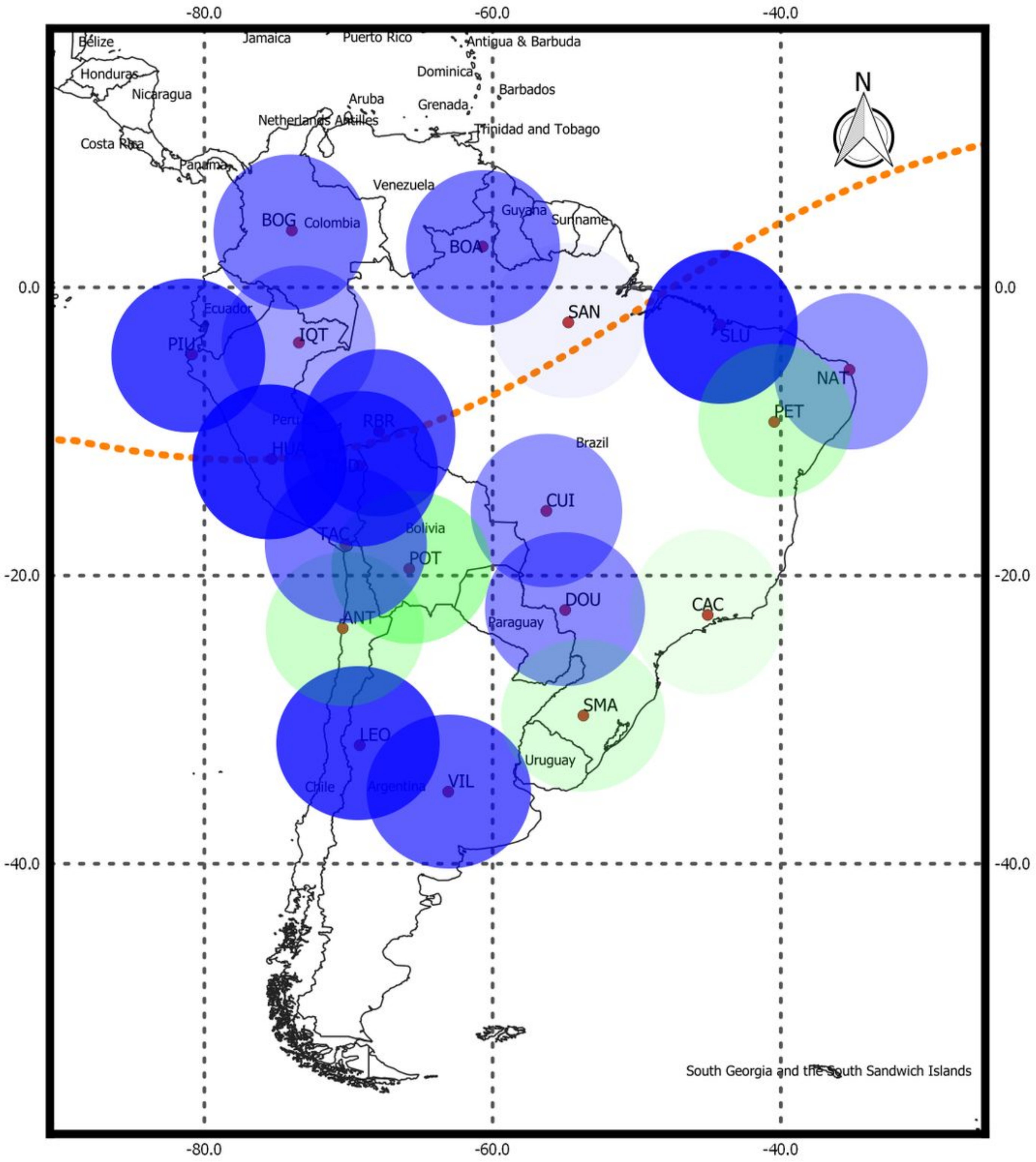

Figure 1

Map: Map showing the locations of the GPS stations used in this study. The circles represent the area covered by the stations considering an elevation mask of 30° and the dashed orange line refers to the magnetic equator, provided by the International Geomagnetic Reference Field (IGRF‐12) model for the year 2015. The opacity of circles increases with the GPS data availability during the solar cycle 24. Note: The designations employed and the presentation of the material on this map do not imply the expression of any opinion whatsoever on the part of Research Square concerning the legal status of any country, territory, city or area or of its authorities, or concerning the delimitation of its frontiers or boundaries. This map has been provided by the authors.

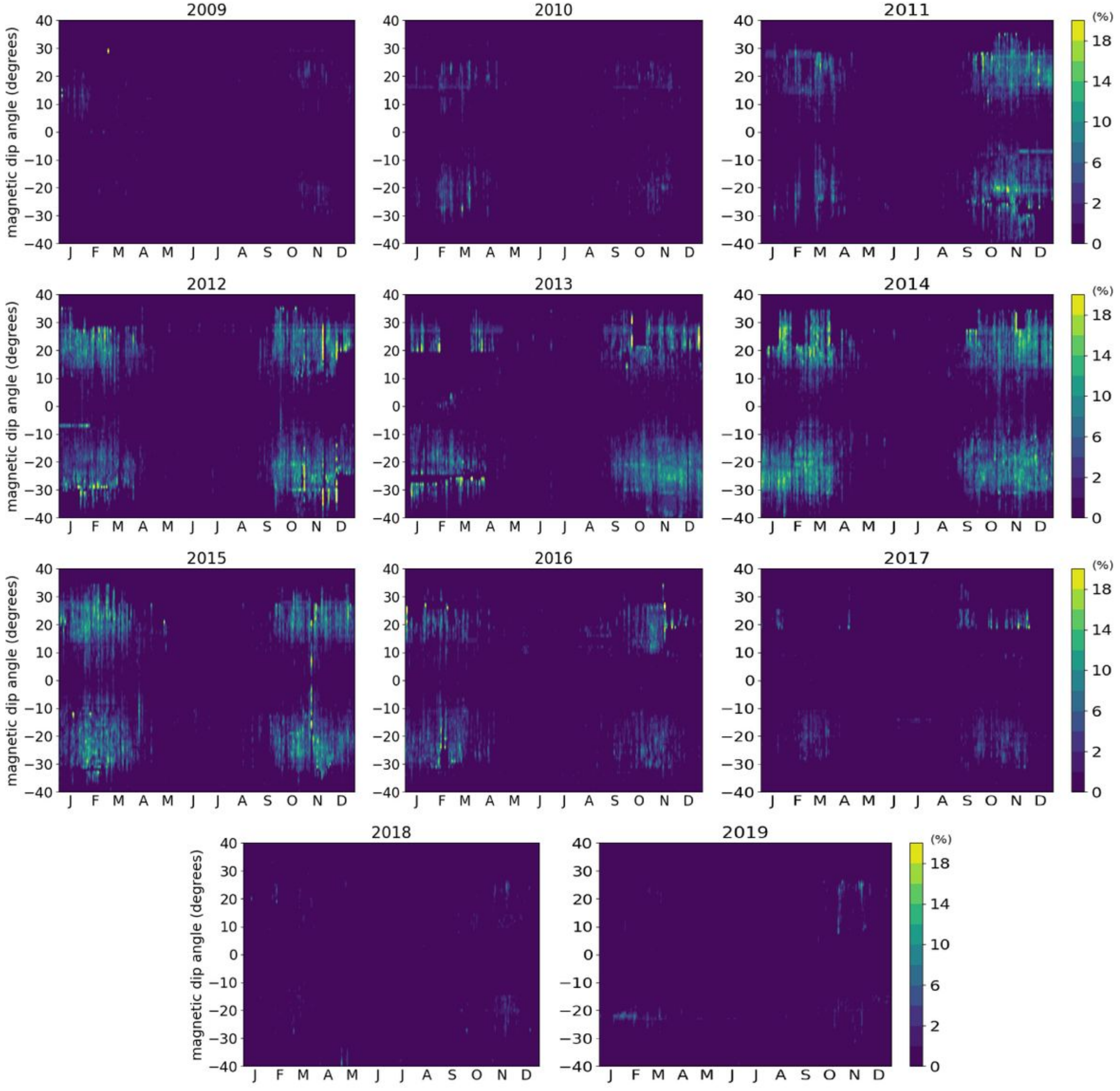

Figure 2

Full characterization: Occurrence of S4 index above 0.2 for full solar cycle 24 (2009-2019) as function of magnetic dip angle and month.

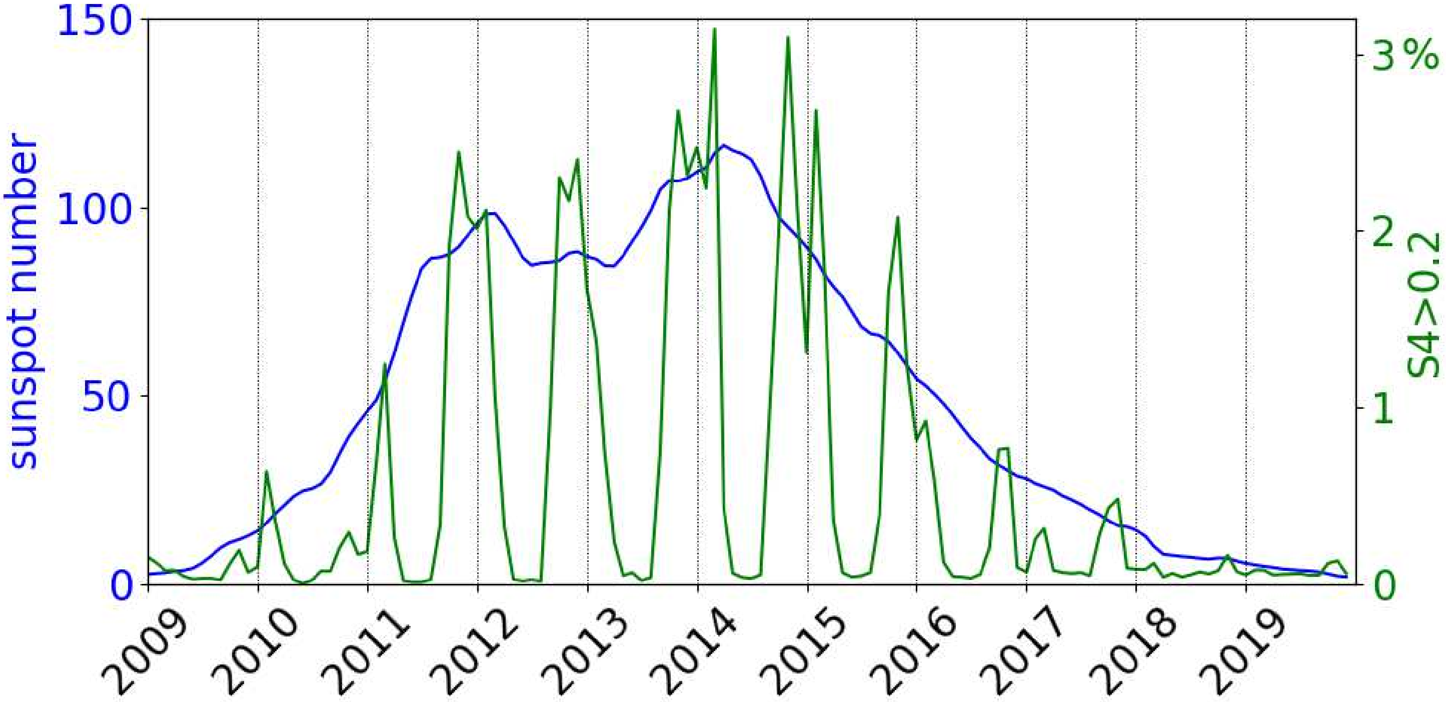

Figure 3

Solar cycle 24: Progression of the solar cycle 24, according to monthly smoothed sunspot number and monthly percentage of S4 over 0.2.

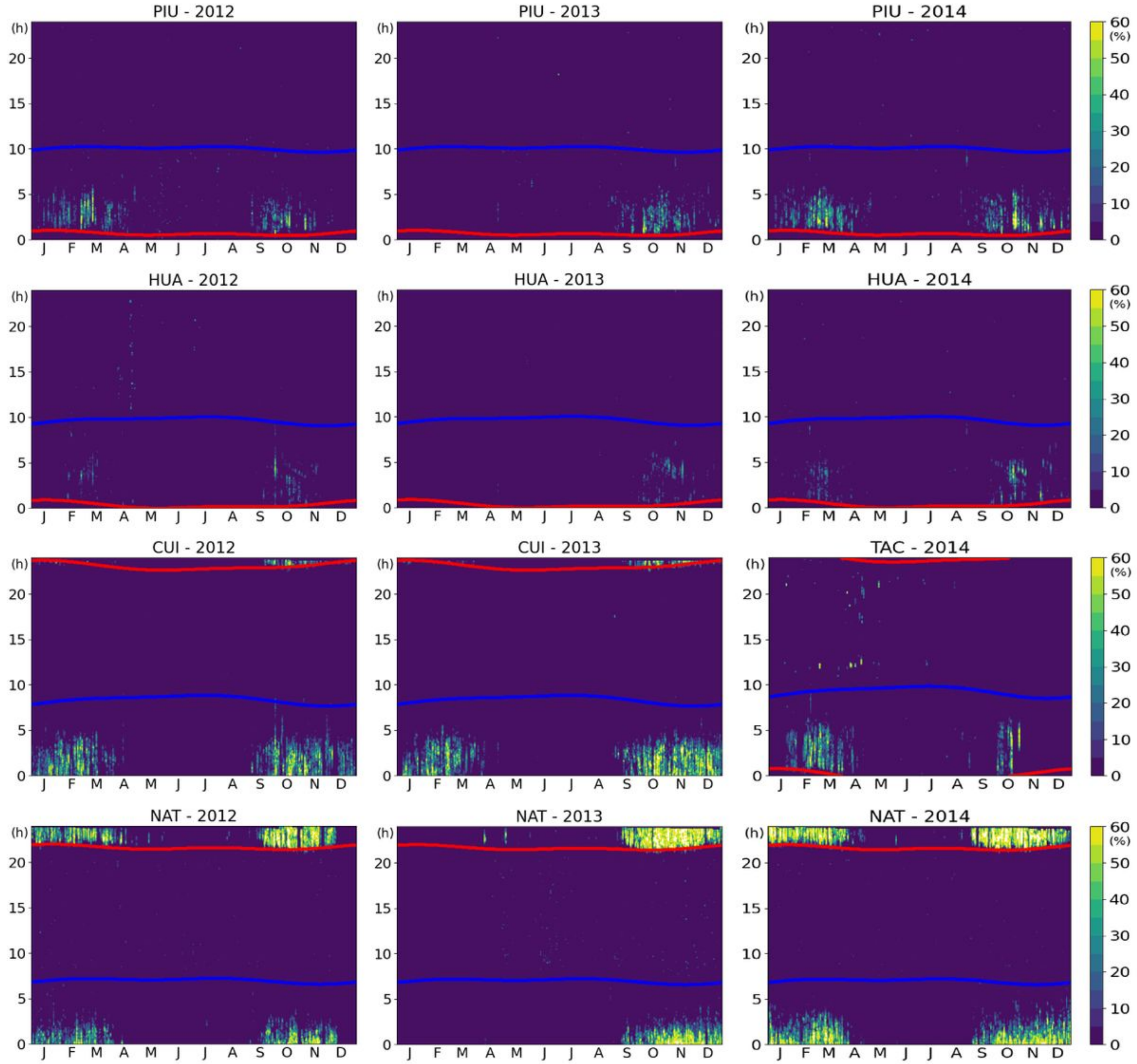

Figure 4

Daily variation: Occurrence of S4 index above 0.2 for solar maximum conditions (2012 to 2014) as a function of the hour of the day (in UT) and of the month. Blue lines indicate the sunrise, while red lines indicate the sunset, both expressed at 350 km.

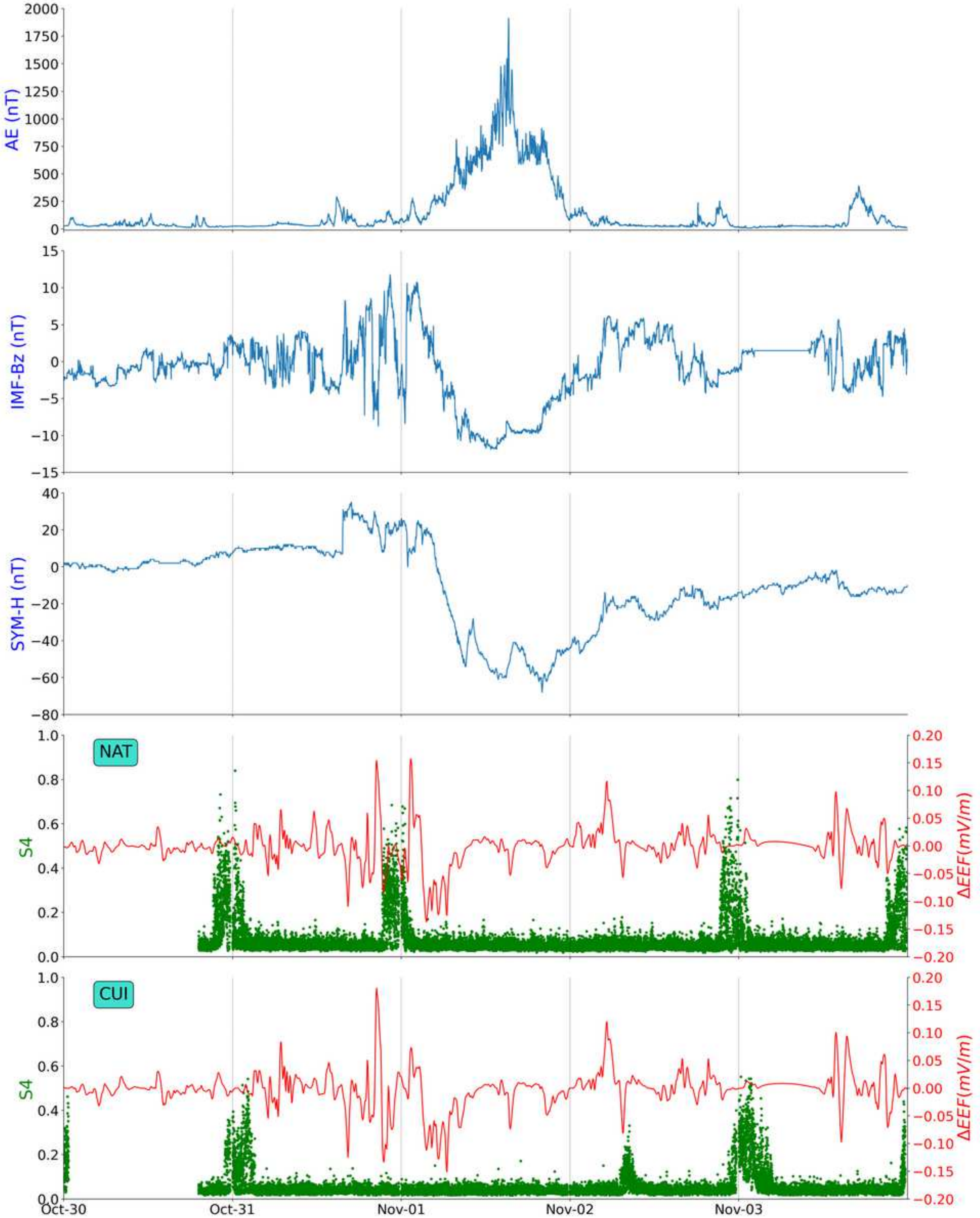

Figure 5

Event 2012: AE, IMF-Bz, SYM-H, and S4 indexes and ΔEEF at NAT and CUI stations, from October 30, 2012 to November 03, 2012. Time in UT.

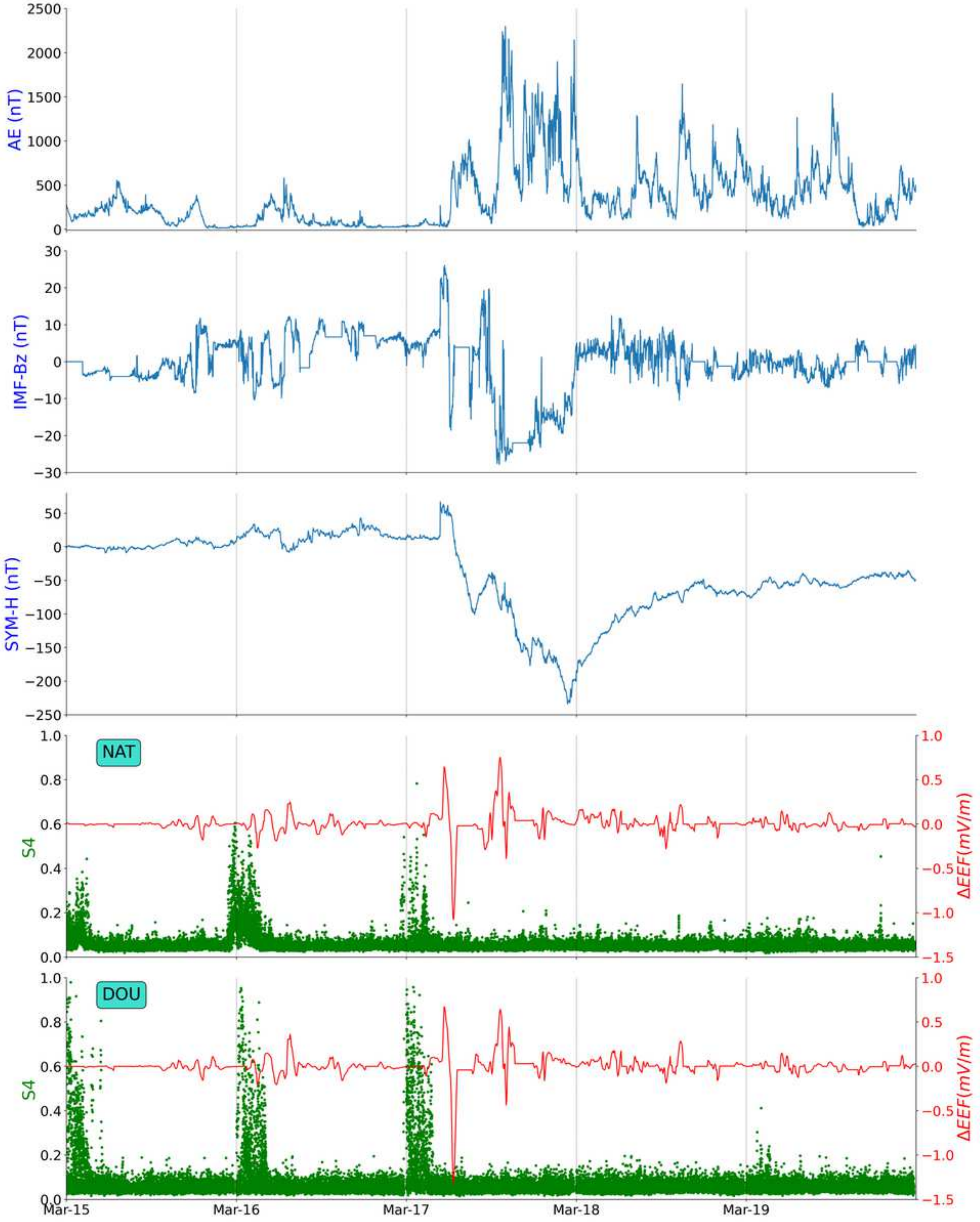

Figure 6

Event 2015: Same as Figure 5, from March 15, 2015 to March 19, 2015.

Supplementary Files

This is a list of supplementary files associated with this preprint. Click to download.

- Graphicalabstractimage2.jpg